Topological electromotive force from domain-wall dynamics in a ferromagnet

Shengyuan A. Yang,[1] Geoffrey S. D. Beach,[1,2] Carl Knutson,[1] Di Xiao,[1,3] Zhenyu Zhang,[3] Maxim Tsoi,[1] Qian Niu,[1] A. H. MacDonald,[1] and James L. Erskine[1]

[1]*Department of Physics, The University of Texas, Austin, Texas 78712-0264, USA*

[2]*Department of Materials Science and Engineering, MIT, Cambridge, Massachusetts 02139, USA*

[3]*Materials Science & Technology Division, Oak Ridge National Laboratory, Oak Ridge, Tennessee 37831, USA*

(Received 12 May 2010; revised manuscript received 12 July 2010; published 10 August 2010)

We formulate a local gauge-invariant theory for the electromotive force induced by domain-wall dynamics in a ferromagnet. We demonstrate that this emf generation is a real-space topological pumping effect. The integral of the emf over one pumping period is a quantized topological invariant which does not depend on the details of the domain-wall configuration nor on its detailed dynamics. Based on our theory, the full instantaneous electric potential distribution can be mapped out by standard electrostatic methods. We also provide further details on our recent experiments which confirmed the emf induced by domain-wall dynamics.

DOI: 10.1103/PhysRevB.82.054410 PACS number(s): 75.47.−m, 75.60.Ch, 72.25.Ba, 75.75.−c

I. INTRODUCTION

Because of its importance in information storage and processing technology, the interplay between charge transport and magnetization dynamics has been a subject of extensive research during past two decades. One celebrated accomplishment is the discovery of giant magnetoresistance in magnetic multilayer structures. A related effect is the change in resistance due to the presence of a static domain wall (DW) in a magnetic nanowire.[1–4] When subjected to a large electric current the DW can be driven by spin-transfer torques to move within the nanowire.[5–22] The ability to manipulate DW positions and displacements on a nanometer scale via spin torque interactions has obvious technological implications which continue to drive scientific interest in current driven DW phenomena.

The inverse of this effect, i.e., the appearance of an emf generated by a DW propagating through a ferromagnetic material, known as ferro-Josephson effect, was predicted by Berger in 1986.[23] After two decades, this effect was finally observed experimentally and has been reported in our previous publication.[24]

Theoretically, Berger's original result has been rederived via several different approaches.[24–32] Barnes and Maekawa showed that the emf is related to the spin Berry phase[33] of the adiabatic transport of a conduction electron around a loop.[26,34] Saslow derived this result from a nonequilibrium thermodynamic approach.[27] Duine started from a functional-integral method and investigated the role played by nonadiabatic and spin-relaxation processes in this effect,[29,30] also carefully studied by Tserkovnyak and Mecklenburg.[31] Numerical studies on this effect have been performed by Stamenova *et al.* In our previous work,[24,28] we have shown that this emf is due to the Berry curvatures experienced by conduction electrons in a spin texture that varies in space and time. We developed a local gauge-invariant formalism for studying the induced potential distribution for general local spin dynamics. As a result, we discovered a universal relationship between the emf and the frequency of DW precession, which has been successfully verified by our experiment.[24]

Due to length restrictions, several important details were not fully discussed in our previous work. In the present paper, we would like to not only address these details but also extend our previous work. We show that the ferro-Josephson effect is one particular example of a class of real-space topological pumping effects. The manifestation of its topological nature is that the integral of the pumped emf over one pumping cycle is a quantized topological invariant equal to integer multiples of h/e. We demonstrate that our theory combined with standard electrostatic methods is capable of calculating the full chemical-potential distribution induced by general local spin dynamics. The first experimental detection of this effect is also reviewed in detail.

Our paper is organized as following. In Sec. II, starting from a set of semiclassical equations of motion for electron wavepackets, we show that the DW-induced emf is a special example of topological pumping in real space. In Sec. III, we provide a topological argument for the DW-induced emf that is valid for any type of DW. In Sec. IV, we discuss our method to solve for the chemical-potential distribution induced by general local spin dynamics. Section V describes a recent experimental detection of this emf. In Sec. VI, we summarize our results and discuss our conclusions.

II. BERRY CURVATURE AND TOPOLOGICAL PUMPING

The Berry phase is a geometric phase that a state acquires during adiabatic evolution of the system in some parameter space.[33] Berry phases not only lead to interference patterns, as in the Aharonov-Bohm effect but also have direct influence on the dynamics of the system. Consider an electron wavepacket evolving in a single Bloch band of a crystal. Under a perturbation that is slowly varying in space and time, interband transitions are suppressed exponentially. The resulting adiabatic evolution of the wavepacket in phase space gives rise to various interesting Berry phase effects. Sundaram and Niu[35] have derived a set of semiclassical equations of motion which describe the time evolution of the phase-space center $(\mathbf{r}_c, \mathbf{k}_c)$ of the wavepacket in a single Bloch band,

$$\dot{\mathbf{r}}_c = \frac{\partial \mathcal{E}}{\hbar\, \partial \mathbf{k}_c} - (\overleftrightarrow{\Omega}_{\mathbf{kr}} \cdot \dot{\mathbf{r}}_c + \overleftrightarrow{\Omega}_{\mathbf{kk}} \cdot \dot{\mathbf{k}}_c) - \mathbf{\Omega}_{\mathbf{k}t}, \tag{1}$$

$$\dot{\mathbf{k}}_c = -\frac{\partial \mathcal{E}}{\hbar\, \partial \mathbf{r}_c} + (\overleftrightarrow{\Omega}_{\mathbf{rr}} \cdot \dot{\mathbf{r}}_c + \overleftrightarrow{\Omega}_{\mathbf{rk}} \cdot \dot{\mathbf{k}}_c) + \mathbf{\Omega}_{\mathbf{r}t}, \tag{2}$$

where $\mathcal{E}(\mathbf{r}_c, \mathbf{k}_c)$ is energy of the wavepacket and $\overleftrightarrow{\Omega}$s are Berry curvature tensors defined in terms of the gauge potentials $\mathcal{A}$ known as Berry connections,

$$\mathcal{A}_{k_\alpha} = i\langle u|\frac{\partial}{\partial k_\alpha}|u\rangle, \quad \mathcal{A}_{r_\alpha} = i\langle u|\frac{\partial}{\partial r_\alpha}|u\rangle, \tag{3}$$

where $\alpha = 1,2,3$ labels the three space components of a vector (hereafter we shall drop the subscript c referring to the wavepacket center when appropriate) and $|u\rangle$ is the periodic part of the local Bloch eigenstate for this band.[35] The Berry curvatures correspond to the gauge fields associated with these gauge potentials. For example,

$$\overleftrightarrow{\Omega}_{k_\alpha r_\beta} = \frac{\partial}{\partial k_\alpha}\mathcal{A}_{r_\beta} - \frac{\partial}{\partial r_\beta}\mathcal{A}_{k_\alpha}, \tag{4a}$$

$$\Omega_{r_\alpha t} = \frac{\partial}{\partial r_\alpha}\mathcal{A}_t - \frac{\partial}{\partial t}\mathcal{A}_{r_\alpha}. \tag{4b}$$

All other Berry curvatures are defined in a similar way.

The Berry curvature fields are gauge-invariant physical quantities. Each individual term in the above equations of motion can have significant influence on the dynamics of electrons in appropriate contexts. The term with k-space Berry curvature $\overleftrightarrow{\Omega}_{\mathbf{kk}}$ represents an anomalous velocity. It is the origin of the intrinsic contribution to the anomalous Hall effect and spin Hall effect.[36] The term $\mathbf{\Omega}_{\mathbf{k}t}$, which arises when the system depends on certain time-varying parameters, leads to a charge pumping effect.[37] Consider the simplest case of a band insulator along x axis with a single fully occupied band. When the system has some parameter that is periodically varying in time, a quantized charge can be pumped through the system over one period T,

$$Q = \int_0^T dt\mathbf{j} = e\int_0^T dt \int_{BZ} \frac{dk_x}{2\pi}\Omega_{k_x t} = eC, \tag{5}$$

where BZ denotes the Brillouin zone, $(-e)$ is the electron charge, and C is an integer known as the first Chern number. This quantization is due to the topology of (k,t) space which forms a closed surface. The Chern number C, corresponding to the curvature field integrated over this closed surface, gives the topological charge enclosed by the surface.

The last term $\mathbf{\Omega}_{\mathbf{r}t}$ in Eq. (2), which is the counterpart of $\mathbf{\Omega}_{\mathbf{k}t}$, is the focus in this paper. While the $\mathbf{\Omega}_{\mathbf{k}t}$ term pumps a current, the $\mathbf{\Omega}_{\mathbf{r}t}$ term pumps an emf. Observe that $\hbar\dot{k}_c$ being the rate of change in momentum, is just the force acting on the electron, hence $\mathbf{\Omega}_{\mathbf{r}t}$ constitutes a local force field. Work is required to move electrons around in this force field. Therefore the emf along some path l can be calculated from

$$\text{emf} = -\frac{\hbar}{e}\int_l d\mathbf{r} \cdot \mathbf{\Omega}_{\mathbf{r}t}. \tag{6}$$

Because this approach is local and gauge invariant from the very beginning, it is physically transparent and does not involve elusive concepts such as the Berry phase on an open path. Furthermore, a comparison between Eqs. (5) and (6) makes it natural to anticipate that there is also a topological invariant associated with the time integral of the emf in one period, as we discuss in the following section.

III. PUMPED EMF: TOPOLOGICAL ARGUMENT

Domain walls in ferromagnetic materials are transition regions that separate domains with different locally metastable magnetizations. Usually the magnitude of the order parameter is assumed to be fixed, and only its direction varies in space. Hence we can introduce a local magnetization orientation vector $\hat{\mathbf{n}}(\mathbf{r},t)$. We take the orientation of the local exchange field, which captures the influence of magnetic order on the fermionic quasiparticles, to be parallel to the magnetization orientation vector. For notational concreteness we will assume a s-d model in which we invoke a magnitude S of the local d spin that is exchange coupled to itinerant s electrons that are responsible for transport. In a coordinate representation, the itinerant electron mean-field Hamiltonian is

$$H_{\text{sd}} = -J\hat{\mathbf{n}}(\mathbf{r},t) \cdot \boldsymbol{\sigma}, \tag{7}$$

where $\boldsymbol{\sigma}$ denotes the conduction-electron spin and J is the exchange coupling strength. The typical coupling energy $J(\sim 1$ eV) is large, such that the conduction-electron spin will adiabatically follow the direction $\hat{\mathbf{n}}$ during its evolution. Therefore, when $\hat{\mathbf{n}}(\mathbf{r},t)$ varies in space and time, it will generate Berry curvature fields acting on the conduction electrons.[38]

In ferromagnetic nanowires, the magnetization easy axis is usually along the wire. Hence on the two sides of the domain wall the magnetic domains have opposite magnetization directions. Then the direction of $\hat{\mathbf{n}}$ is fixed at the two ends, for example,

$$\hat{\mathbf{n}}(x = -\infty) = -\hat{\mathbf{e}}_x, \quad \hat{\mathbf{n}}(x = +\infty) = +\hat{\mathbf{e}}_x. \tag{8}$$

This constraint determines the topology of the system and we shall see that it plays an essential role in our topological argument. The configuration described by Eq. (8) is known as a tail-to-tail configuration. A head-to-head configuration corresponds to reversing the signs of the vectors $\hat{\mathbf{e}}$. The following argument applies to both configurations.

In order to easily picture the pumping process, let us first consider a transverse DW. The local spin direction $\hat{\mathbf{n}}$ of a transverse wall depends only on one coordinate x (see Fig. 1). Hence it is also known as the one-dimensional (1D) DW.

The dynamics of DW can be induced by various means. The simplest way is to drive the DW by a static uniform magnetic field. At low fields, the DW makes a rigid translational motion like a soliton. When the field is above the so-called Walker breakdown field,[39] the local spins begin to

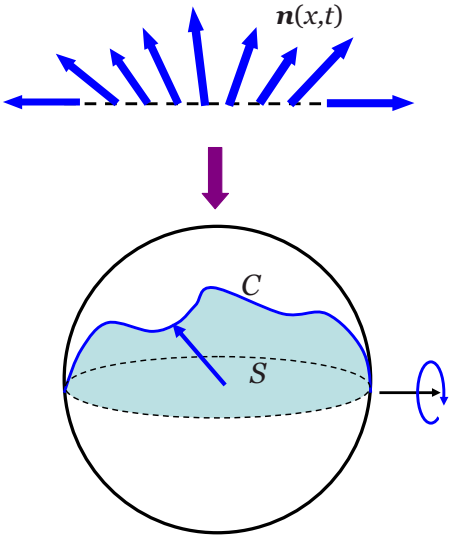

FIG. 1. (Color online) (Up) Local spin configuration for a 1D DW at an instant of time. (Bottom) A curve $\mathcal{C}$ is traced out by $\hat{\mathbf{n}}$ on the surface of a unit sphere. $\mathcal{S}$ is the shaded area bounded by $\mathcal{C}$ and the half equator. When the DW precesses, the area $\mathcal{S}$ changes with time. During one pumping period, the area swept by $\mathcal{C}$ is 4π.

precess around the field, causing the entire DW to precess periodically during its translation. If we look at the curve $\mathcal{C}[\hat{\mathbf{n}}]$ traced out by the vector $\hat{\mathbf{n}}(x,t)$ on a unit sphere, this DW precession can be pictured as a "rope-skipping" process of the curve $\mathcal{C}$, as shown in Fig. 1.

The Berry curvature field Ω_{xt} is calculated from the definition Eqs. (3) and (4b) with $|u\rangle=|\psi\rangle\otimes|\chi\rangle$, where $|\psi\rangle$ is the orbital part of the eigenstates wave function and $|\chi\rangle=|\hat{\mathbf{n}},\pm\rangle$ is its spin part. Due to the large energy difference $2J$ between the two spin states $|\hat{\mathbf{n}},\pm\rangle$, the transition between them are suppressed and each sector can be considered separately under adiabatic approximation. In the following discussion, we only consider the spin majority carriers with $|\chi\rangle=|\hat{\mathbf{n}},+\rangle$ as in the half metal limit. The discussion is easily extended to include the spin minority carriers and this will be done at the end of Sec. IV.

Parameterizing $\hat{\mathbf{n}}(x,t)$ by spherical angles (θ,ϕ), the Berry curvature field takes the following form:

$$\Omega_{xt}=\frac{1}{2}\sin\theta\left(\frac{\partial\theta}{\partial t}\frac{\partial\phi}{\partial x}-\frac{\partial\theta}{\partial x}\frac{\partial\phi}{\partial t}\right). \tag{9}$$

The emf along the wire can be obtained by a direct integration,

$$\text{emf}=-\frac{\hbar}{e}\int_{-\infty}^{\infty}dx\Omega_{xt}=\frac{\hbar}{2e}\frac{d}{dt}\int_{\mathcal{C}}\cos\theta d\phi, \tag{10}$$

where in the second step the integrand is evaluated over the curve $\mathcal{C}[\hat{\mathbf{n}}]$. The two ends of $\mathcal{C}$ are pinned at two opposite poles intersecting with the x axis due to the constraint of Eq. (8). Due to the presence of the time derivative, the integral in Eq. (10) is equal to a contour integral along the boundary of the surface region $\mathcal{S}$ enclosed by $\mathcal{C}$ and any fixed (time independent) curve on the sphere. Let us take the curve to be the half equator, as indicated in Fig. 1. By Stokes' theorem, the contour integral can be turned into a surface integral which equals the area of $\mathcal{S}$,

$$\text{emf}=-\frac{\hbar}{2e}\frac{d}{dt}\int\int_{\mathcal{S}}d\cos\theta\wedge d\phi=-\frac{\hbar}{2e}\frac{d}{dt}\text{Area}(\mathcal{S}). \tag{11}$$

This expression is nonzero when the area of $\mathcal{S}$ is time dependent. Therefore an emf can be generated when the curve sweeps over the spherical surface in time, i.e., when the DW precesses, such as being driven by a magnetic field above the Walker breakdown. In one period, the area swept by the curve is an integer multiples of 4π. Therefore the integral of the pumped emf over one period is a topological invariant,

$$\int_0^T dt\,\text{emf}=\frac{h}{e}C,\quad C\in\mathbb{Z}. \tag{12}$$

For the simple transverse wall precession as depicted in Fig. 1, we should have $C=-1$.

At first glance, it might appear that the integral of curvature Ω_{xt} over the (x,t) manifold should not be quantized because the manifold is not closed, i.e., the system configuration at $x=-\infty$ differs from that at $x=+\infty$. However, as we have shown above, the real topology of this problem is of a closed spherical surface together with the essential constraint Eq. (8) that fixes the ends of the curve $\mathcal{C}$ on this surface. The pumping is realized by the rope-skipping movement of the curve $\mathcal{C}$ explained above.

According to this argument, the average emf over one period should simply be

$$\overline{\text{emf}}=\frac{\hbar}{e}\omega C. \tag{13}$$

Here the pumping frequency ω is the frequency of the DW precession. It is clear that this result does not depend on the detailed DW profile nor on details of its dynamical evolution, justifying our contention that it is a topological pumping effect.

In a previous work by Barnes *et al.*,[25] the authors argued that the emf is a consequence of the release of magnetostatic energy as the DW propagates under the influence of a magnetic field. However, the above analysis shows that topological pumping is related to DW precession only (or more generally to wall dynamics) and has nothing directly to do with the DW displacement. For example, for a moving DW without precession, which occurs when the DW is driven by a magnetic field below Walker breakdown, there should be no emf induced by the topological pumping. In contrast, if one manages to establish a DW pinned in space but free to precess, then it can also pump the same emf as in Eq. (13). This situation is analogous to the spin-pumping effect in magnetic multilayer structures.[40,41]

The analysis above is readily extended to general types of DWs. Numerical simulations of the spin distributions within DWs of soft magnetic nanowires having different cross-sectional dimensions show that transverse wall structure are only stable in narrow wire geometry but that vortex, double vortex, and more complex structures form in wider wire

structures.[42–44] Each vortex DW is characterized by two integers p the polarization and q the vorticity. $p=\pm 1$ indicates whether $\hat{\mathbf{n}}$ in the vortex core is pointing upward or downward and $q=\pm 1$ is the winding number of $\hat{\mathbf{n}}$ around the vortex core. (Textures with $q=-1$ are sometimes referred to as *antivortex* in the literature.) Pumping is induced when the vortex reflects periodically back and forth between the two wire edges. Such a situation can be realized, for instance, by a driving magnetic field above a critical field which is also termed as Walker breakdown field. Oscillatory field-driven vortex DW motion has been studied using numerical simulations and has been detected by recent experiments.[45–48] During the periodic oscillation along transverse direction, each time the vortex core encounters the edge, its polarization p will change sign while the winding number q is preserved.[46,47,49]

The pumped emf between the two ends is obtained by integrating the force field $\mathbf{\Omega}_{\mathbf{r}t}$ along a line connecting the two ends, e.g., for the line $y=0$. Again we can map the unit vector $\hat{\mathbf{n}}$ on this line to a curve on the unit sphere and repeat our rope-skipping argument. However, unlike the transverse wall case, the movement of the curve $\mathcal{C}$ is not due to the precession of the wall plane but is triggered by the transverse motion of the vortex core. Before the vortex core hits the line, the curve $\mathcal{C}$ lies on the equator. When the core is passing across the line, $\mathcal{C}$ moves out of the xy plane since the vector $\hat{\mathbf{n}}$ in the core has a finite z component. After the traversing process is complete, an area equal to half the spherical surface is swept by $\mathcal{C}$. The other half of the spherical surface is swept when the core bounces back from the edge with a reserved polarity. Again the integral of the pumped emf over one period leads to a quantized topological invariant and the average emf is the same as Eq. (13) with ω being the frequency for the transverse motion of the vortex core.

The above discussion demonstrates the power of an approach based on topology that makes it possible to deal with arbitrary DW geometries with a unified approach. In the following, we treat the vortex DW case using an alternative approach which illustrates the connection between the pumped emf and the topology of the vortex more clearly. For one period, we assume that the vortex starts out from the upper edge, travels across the strip, gets bounced back by the lower edge, and returns to the upper edge. Let $\mathbf{X}=[X(t),Y(t)]$ denote the position of the vortex center and $\mathbf{v}=(\dot{X},\dot{Y})$ its velocity. Notice that the Berry curvatures depend on space and time only through $[x-X(t)]$ and $[y-Y(t)]$. The time integral of the emf over the first half period can be converted to a surface integral,

$$\int_0^{T/2} dt\ \mathrm{emf} = -\frac{\hbar}{e}\int_0^{T/2} dt \int_{-\infty}^{\infty} dx \Omega_{xt}$$

$$= -\frac{\hbar}{e}\int\int dxdy\Omega_{xy}, \tag{14}$$

where the r-space Berry curvature Ω_{xy} when written in terms of spherical angles is

$$\Omega_{xy} = \frac{1}{2}\sin\theta(\nabla\theta\times\nabla\phi)\cdot\hat{\mathbf{e}}_z, \tag{15}$$

which is related to the gyrovector in the discussion of Bloch line dynamics.[50] It is well known that the surface integral of the Berry curvature Ω_{xy} for a vortex gives a topological invariant called the Skyrmion charge of the vortex[51] which does not depend on the detailed profile of the DW,

$$\int\int dxdy\Omega_{xy} = \pi pq. \tag{16}$$

So we observe immediately that the time integral of the emf [Eq. (14)] is again a quantized value. As for the second half period, the vortex moves in the opposite transverse direction, however, p also changes sign, so the integral of emf over the second half period is the same as that for the first half. Furthermore because v_y has the same sign as pqv_x,[47] the sign of emf is determined after specifying the direction of the longitudinal motion of the vortex. Hence, for a vortex DW propagating from left to right, we recover the result $\mathrm{emf}=-(\hbar/e)\omega$.

It should be emphasized that the local approach based on Berry curvatures is a gauge-invariant theory from the very beginning, unlike approaches based on Berry phases or Berry connections which always need a gauge fixing step. In the original work by Berger,[23] the force takes a form of spatial gradient because a gauge has been implicitly chosen such that $\mathcal{A}_x=0$. In the work by Barnes and Maekawa,[26] the gauge has been fixed in another way such that $\mathcal{A}_t=0$ at $x=\pm\infty$.

The topological argument presented above [with the relation Eq. (12)] is a significant result which goes beyond our previous discussion in Ref. 24. From this argument, we can see immediately that the average emf is given by a universal Josephson-type relation which only depends on the frequency of the DW transformation. If we measure the voltage drop along the direction of DW motion, then an average voltage drop of $\hbar\omega/e$ should be detected.

IV. GENERAL METHODS TO SOLVE FULL CHEMICAL-POTENTIAL DISTRIBUTION

Starting from our local formalism, it is easy to identify the topology of the system and calculate the pumped emf. These are global properties of the system. However, the real power of a local approach is that it also enables us to study various local properties, such as the full instantaneous chemical-potential distribution produced by the local spin dynamics.

The starting point is the Boltzmann equation for the phase-space distribution function $g(\mathbf{r},\mathbf{k},t)$ in the relaxation time approximation,

$$\frac{dg}{dt} = -\frac{g-f}{\tau}, \tag{17}$$

where τ is the relaxation time and

$$f(\mathbf{r},\mathbf{k}) = \frac{1}{e^{[\mathcal{E}(\mathbf{r},\mathbf{k})-\mu(\mathbf{r})]/k_BT}+1} \tag{18}$$

is the local Fermi distribution function appropriate for the electron energy $\mathcal{E}$ and the chemical potential μ at the position

r. The distribution function g can be solved as

$$g = f - \int_{-\infty}^{t} dt' e^{-(t-t')/\tau} \left[\dot{\mathbf{r}} \cdot \frac{\partial}{\partial \mathbf{r}} + \dot{\mathbf{k}} \cdot \frac{\partial}{\partial \mathbf{k}} \right] f. \tag{19}$$

Assuming that the semiclassical dynamics is much slower than the relaxation time, which is usually the case in metals, the time integral can be carried out directly. The $\dot{\mathbf{r}}$ and $\dot{\mathbf{k}}$ above can be substituted from the semiclassical equations of motion Eqs. (1) and (2). Here we neglect the spin-orbit coupling, hence the term $\Omega_{\mathbf{k}t}$ in Eq. (1) vanishes. We then find that the terms involving derivatives of $\mathcal{E}$ get canceled out and we are left with

$$g = f - \tau \dot{\mathbf{r}} \cdot (\nabla \mu - \hbar \mathbf{\Omega}_{\mathbf{r}t}) \frac{\partial f}{\partial \mu}. \tag{20}$$

In the steady state the transport current of an open system must be zero at every point in space. Hence the irrotational part of the field $\hbar \mathbf{\Omega}_{\mathbf{r}t}$ has to be balanced by the chemical-potential gradient $\nabla \mu$. In experiment, what we really measure is the difference of chemical potentials between two points. The voltage signal read from a voltmeter is connected to the chemical-potential difference $\Delta \mu$ through the relation

$$V = -\Delta \mu / e. \tag{21}$$

Note that we are using the word chemical potential in our discussion to include both electrical potential contributions that bend the conductor's bands and Fermi energy contributions that establish the position of the chemical potential within those bands. In metals the Fermi energy variation is always negligible so that the chemical-potential variation is in fact essentially equal to the electrical potential variation. In this way, the measured voltage signal reflects the emf induced by the topological pumping term $\mathbf{\Omega}_{\mathbf{r}t}$.

The full chemical-potential distribution can therefore be solved from the Poisson equation,

$$\nabla^2 \mu = \hbar \nabla \cdot \mathbf{\Omega}_{\mathbf{r}t} \tag{22}$$

subjected to the Neumann boundary condition.[52] This can be understood by noticing that in the equation of motion [Eq. (1)], the $\mathbf{\Omega}_{\mathbf{r}t}$ acts as an effective electric field (while the field $\Omega_{xy}\hat{\mathbf{e}}_z$ is an effective magnetic field). The divergence of the force field on the right-hand side therefore plays the role of source charge densities. At this stage, the problem of calculating μ has been completely mapped into a standard electrostatic problem hence can be attacked by utilizing well-developed techniques.[24,28,53]

Before proceeding, we would like to address an issue related to the measurement. When the DW is driven by a constant applied magnetic field, the possibility that coupling between the external field and the conduction-electron spin, the Zeeman energy term, could affect the measured voltage signal arises as an interesting issue. The Zeeman energy is part of the total energy $\mathcal{E}(\mathbf{r},\mathbf{k})$, and from the analysis above, it is clear that the spatial variation in $\mathcal{E}$ does not contribute to the chemical-potential gradient in the steady state. Therefore the measured voltage signal should not be affected by the Zeeman energy term.

In the following, using the vortex DW as an example, we details how the potential distribution is calculated. The curvature field $\mathbf{\Omega}_{\mathbf{r}t}$, when written in terms of spherical angles, is[54]

$$\mathbf{\Omega}_{\mathbf{r}t} = \frac{1}{2} \sin\theta \left(\frac{\partial \theta}{\partial t} \nabla \phi - \frac{\partial \phi}{\partial t} \nabla \theta \right). \tag{23}$$

For a vortex DW, θ and ϕ only depend on time through the combination $[x - X(t)]$ and $[y - Y(t)]$ where (X,Y) is the center of the vortex core as defined in the previous section. We find that

$$\mathbf{\Omega}_{\mathbf{r}t} = -\Omega_{xy} \hat{\mathbf{e}}_z \times \mathbf{v}, \tag{24}$$

which mimics the relation between electric field and magnetic field. The charge density on the right-hand side of Eq. (22) is peaked around the DW and vanishes in a uniform domain. The potential and field outside the DW region can be calculated by a standard multipole expansion method.

For regions far from the DW (compared with the DW size), only the lowest nonvanishing multipole moment is needed. For the case of vortex DW, it turns out to be the dipole moment,

$$\mathbf{P} = \varepsilon_0 \frac{\hbar}{e} \int d^2 r \mathbf{r} \nabla \cdot \mathbf{\Omega}_{\mathbf{r}t} = -\varepsilon_0 \frac{\hbar}{e} \int d^2 r \mathbf{\Omega}_{\mathbf{r}t}$$

$$= \varepsilon_0 \frac{\hbar}{e} pq\pi \hat{\mathbf{e}}_z \times \mathbf{v}, \tag{25}$$

where we have used Eqs. (16) and (24). The dipole has a magnitude that is proportional to the Skyrmion charge and its direction is perpendicular to the velocity of the vortex core. The dipole distribution is concentrated in the vortex core, which is much smaller than the wire width.[42]

Boundary conditions can be imposed using the image charge method. We replace the boundary condition by image dipoles having mirror symmetry with respect to the two boundaries at $y = +w/2$ and $y = -w/2$ (w is the width of the wire). This creates a line of dipoles on the y axis. At regions far from this line, the source can be approximated by an infinite line of dipoles with an average dipole density $P_x \hat{\mathbf{e}}_x / w$. Hence the voltage difference between $x = -\infty$ and $x = +\infty$ is

$$V_x = \pi pq \frac{\hbar}{e} \frac{v_y}{w}. \tag{26}$$

Since pqv_y has the same sign as v_x, the sign of V_x only depends on the sign of v_x, the direction of DW propagation. Notice that when the vortex core begins to perform zigzag motion at fields above the Walker breakdown field, $\pi |v_y| / w = \omega$. The average voltage drop along the DW propagation direction is therefore just $\bar{V}_x = \hbar \omega / e$, recovering our previous result.

The motion of the vortex along the wire also generates a transverse voltage. For a vortex at the center of the wire, the transverse voltage at the longitudinal position of the vortex is found to be

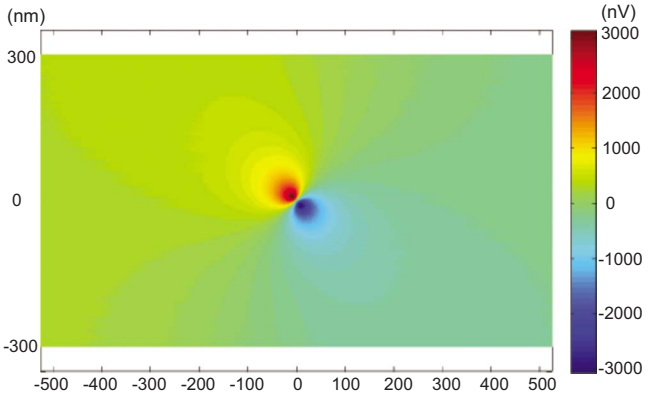

FIG. 2. (Color online) The potential distribution $\mu/(-e)$ calculated numerically from Poisson equation for a vortex at the center of a nanostrip moving with velocity $\mathbf{v}=(150,150)$ m/s. The field distribution closely resembles that for an electric dipole.

$$V_y = \pi \frac{\hbar}{e} \frac{v_x}{w}. \tag{27}$$

When measured through a pair of lateral leads, below breakdown, one should observe a pulse of transverse voltage with the peak value in Eq. (27) and with a time width determine by the wall speed and lead width. Oscillations occur within this pulse above the breakdown when the vortex executes zigzag motion. Each time the vortex collides with a sample edge and gets reflected, V_y will change sign. Therefore, by timing the transverse voltage pulse, one can determine the position and speed of the DW, and by measuring the frequency of the oscillations, one can detect the zigzag motion of the vortex.

Oscillatory DW motion in nanowires has been indirectly measured by magneto-optic polarimetry.[45] The effect is manifested by broadening of the magneto-optic transient produced by a DW sweeping across the probe beam. The voltage method described here offers a direct approach.

In the following, we calculate the full potential distribution by solving the Poisson Eq. (22) directly. In order to do this, we consider a specific DW configuration,

$$\theta(\mathbf{r}) = \frac{\pi}{2}(1 - e^{-|\mathbf{r}-\mathbf{X}|/a}), \tag{28a}$$

$$\phi(\mathbf{r}) = \mathrm{Arg}(\mathbf{r} - \mathbf{X}) + \frac{\pi}{2}, \tag{28b}$$

where a is the radius of the vortex core and the vortex structure is confined within an outer radius R that is comparable to w. Equation (27) specifies a typical vortex with $p=q=1$. The potential distribution $\mu/(-e)$ obtained by solving for the DW configuration numerically is plotted in Fig. 2. In the calculation, we set $w=600$ nm, $a=10$ nm, $R=200$ nm, and $\mathbf{v}=(150,150)$ m/s for a vortex at the center of the strip. Notice that the potential profile indeed coincides with that of an electric dipole pointing in the direction perpendicular to the velocity, as anticipated in Eq. (25).

The DW motion can be driven by various means. In our experiment, we drive a vortex DW by an applied magnetic field. When the applied field H is above the Walker breakdown field, the transformation frequency ω is given by the Larmor frequency $\omega=\gamma H$, where γ is the gyromagnetic ratio.[48,55,56] Therefore the measured voltage should be linear in the applied field $\bar{V}_x/H=(\hbar/e)\gamma \approx 11.6$ nV/Oe (taking spin minority carriers into account will reduce this value by a factor of spin polarization P of the material). This behavior has been confirmed by our experiment,[24] which is discussed at length below.

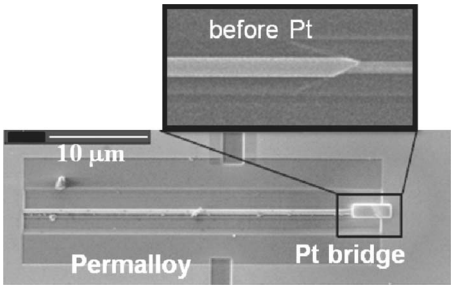

FIG. 3. Scanning electron micrograph of planar nanowire device. Inset shows cut end prior to deposition of Pt bridge.

V. EXPERIMENTAL DETECTION OF EMF GENERATED DURING DOMAIN-WALL MOTION

The emf predicted to develop across a precessing field-driven magnetic DW is small but detectable. In a recent publication,[24] we described the first experimental evidence of this emf. Those experiments and their implications are described in more detail in this section. In order to observe this effect, a thin-film ferromagnetic nanowire structure was fabricated such that a single magnetic DW could be repeatedly nucleated, injected, and driven along the wire in the same direction. By measuring the average voltage that developed along the wire during wall propagation, together with its field dependence, the emf predicted above has been identified and characterized.

The experiments were performed on a planar nanowire patterned from a continuous 20-nm-thick Permalloy ($Ni_{80}Fe_{20}$) film using Ga^+ focused ion-beam (FIB) milling (FEI Strata DB235 dual beam FIB/scanning electron microscopy). The device structure is shown in Fig. 3. The Permalloy film was deposited on a thermally oxidized Si wafer using dc magnetron sputtering. From this film, two parallel trenches were etched away to define a 500-nm-wide and 35 μm long Permalloy stripe (nanowire). At each end of the wire, a large rectangular pad was defined by milling an isolation trench in the film. One end of the nanowire was then milled to a triangular point while the other end remained contiguously joined to the pad. The joined pad region served as a nucleation source for DWs due to its very low coercivity. The tapered geometry at the pointed end of the nanowire wire ensured that DWs would not nucleate within the wire. Hence, magnetic reversal within the wire occurred by the motion of a single magnetic DW, always entering the wire from the injection pad and traveling in the same direction. In order to measure the voltage generated along the wire during

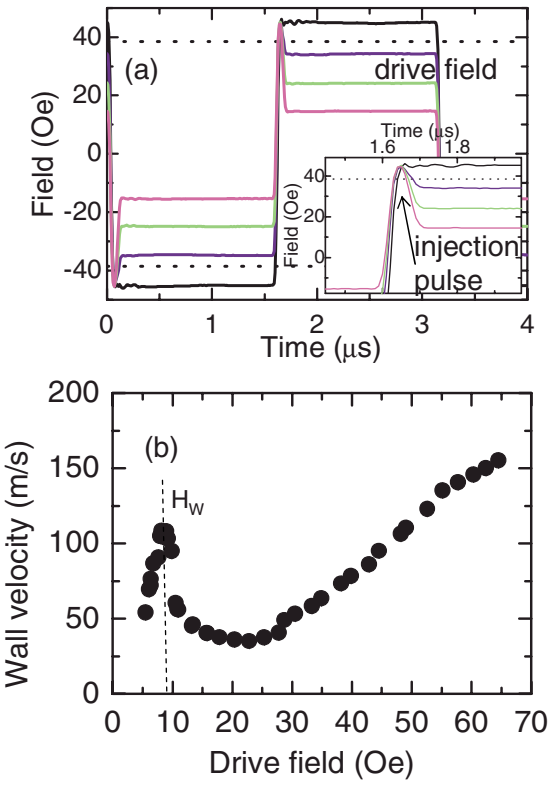

FIG. 4. (Color online) (a) High-frequency drive-field waveforms with 45 Oe injection pulse. Dashed horizontal lines indicate injection field threshold. (b) Measured mobility curve for domain-wall motion in the nanowire.

wall propagation, the pointed end of the nanowire was reconnected to the adjacent pad with a nonmagnetic Pt bridge deposited using electron beam induced deposition in the FIB system. Electrical contacts were then made to the two pads, permitting measurement of the voltage along the nanowire.

Prior to electrical measurements, magnetic DW dynamics in the device were characterized using a high-resolution time-resolved scanning Kerr polarimeter.[57] Domain-wall injection characteristics were first determined by measuring hysteresis loops on both the nucleation pad and the nanowire. The nucleation pad required a magnetic reversal field of ~4 Oe but a field in excess of ~37 Oe was required to inject a nucleated DW from the pad into the nanowire. In order to study DWs in the nanowire driven by a wide range of fields, experiments made use of a wideband rf magnetic field generator integrated into the polarimeter system platform. The magnet produced user-defined field waveforms with risetime of ~20 ns and amplitudes in excess of 65 Oe at the substrate surface. Drive-field waveforms used in this study consisted of square waves of amplitude H_d, with each 1.5 μs plateau preceded by a short 45 Oe "injection pulse." This pulse briefly exceeded the injection field, H_{inj}, injecting the DW and driving it several micrometers into the nanowire before the field amplitude settled to a constant value, H_d. Several such drive-field waveforms are shown in Fig. 4(a). For fields above 45 Oe, no separate injection pulse was required, as a simple square-wave drive field was sufficient for both injection and constant-field drive.

The velocity-field characteristic of DW propagation in the nanowire was measured using a time-of-flight technique as described elsewhere.[58] Average displacement versus time trajectories were recorded using the time-resolved Kerr rotation measured sequentially along the length of wire. The data confirmed that a single DW enters the nanowire from the injection pad and that no nucleation occurred within the wire for the field range used here. The 1.5 μs-long constant-field phase of each drive-field cycle was sufficient to drive an injected DW to the end of the wire. Domain walls were found to propagate for drive fields down to ~5.5 Oe, below which pinning within the nanowire occurred. Our voltage measurements were performed for drive fields well above 5.5 Oe such that there was no pinning of DW in the wire. The average wall velocity in the nanowire versus drive-field amplitude is shown in Fig. 4(b). As expected, the data show two dynamical regimes: a low-field regime with relatively high mobility and a field threshold (the Walker field H_W =8.5 Oe) above which the average wall velocity drops rapidly due to the onset vortex-mediated precessional motion within the DW. It is in this precessional regime that the emf predicted by the theory above is expected to develop.

The most straightforward means of measuring the emf generated during field-driven DW propagation would be to simply monitor the voltage between the two contact pads in time as a DW is launched and driven along the nanowire. However, the high slew-rate magnetic fields used to inject and drive DWs results in a large time-changing magnetic flux through the measurement circuit. The conventional inductive emf in the circuit due to the drive field reaches tens to hundreds of millivolt, many orders of magnitude larger than the emf expected from DW motion. Hence, an alternative approach was developed in order to isolate the small contribution by DW motion to the total measured voltage. The approach relies on an important distinction between conventional inductive (parasitic) emf and the new source of DW-induced emf predicted above. The sign of a purely inductive signal is polarity dependent, i.e., it scales in proportion to the integral of dB/dt through the measurement circuit. The inductive voltage induced by the repetitive drive fields used here should have a time-averaged dc level of zero. However, the emf generated by a propagating DW has a sign that depends only on its direction of propagation. In the device structure used here, a DW always travels in the same direction along the nanowire, regardless of its polarity. By applying a rapid square-wave drive field to repeatedly drive DWs along the wire, a nonzero dc voltage should appear across the wire due to the unidirectional motion of alternately head-to-head and tail-to-tail DWs while the conventional inductive pickup should average to zero.

To detect the small dc voltage level shift that should develop across the wire due to high-repetition rate DW motion along the nanowire, a modulation scheme was employed. The measurements used the DW injection process as a "switch" to periodically turn the DW-induced voltage signal "on" and "off." The experimental approach is outlined in Fig. 5 and made use of field sequence comprised of three components. On top of the continuously running high-frequency drive field (~320 kHz), a low-frequency (317 Hz) square-wave modulation field (amplitude H_m) was superposed. This

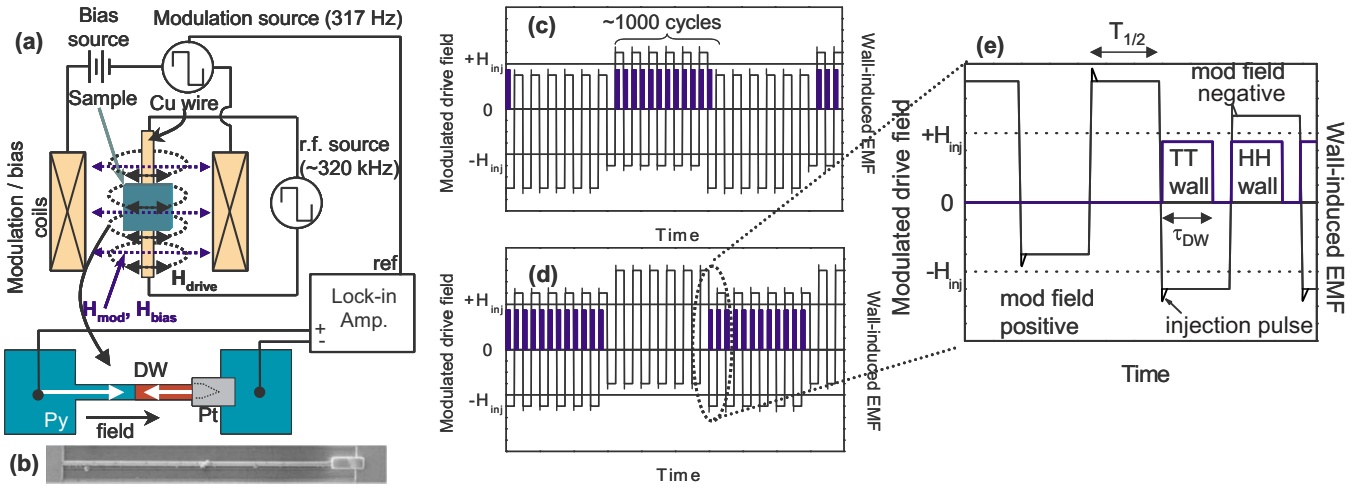

FIG. 5. (Color online) Experiment schematic. (a) Drive, modulation, and bias field configuration with respect to sample. (b) Scanning electron micrograph of nanowire device. [(c) and (d)] Total field waveform for two bias field levels. Injection field H_{inj} indicated by horizontal lines. Black solid lines indicate field waveform; blue indicates voltage signal expected from DW moving along nanowire. (e) Detail of several drive-field cycles immediately before and after a step in the modulation field. Before the step, the nanowire is saturated and no DWs travel along it. After the step, each drive-field half cycle (duration $T_{1/2}$) injects a DW that moves along the wire, generating a voltage until it reaches the end of the wire after a time τ_{DW}.

field was applied by a small air-coil magnet placed as close as possible to the substrate and could reach a maximum field of 11 Oe. Finally, a dc bias field H_{dc} generated by an iron core electromagnet was used to vary the bias level of the time-varying magnetic field waveform.

The sum of these fields as a function of time is shown schematically in Fig. 5 for $H_{dc}=\pm H_m$. For the negatively-biased ($H_{dc}<0$) waveform of Fig. 5(c), a DW is injected and driven across the wire at the beginning of the negative phase of the modulation cycle. Because the positive-going drive-field steps are biased below the DW injection threshold, no further DW motion occurs within the wire until the positive phase of the modulation cycle. During that phase, H_{total} oscillates symmetrically about zero and domain walls, alternately head-to-head and tail-to-tail, are repeatedly injected and driven to the end of the nanowire. Each DW travels in the same direction, leading to a rapid sequence of voltage pulses with the *same* polarity and a nonzero dc level. Hence, the time-averaged dc offset voltage due to high duty cycle repetitive motion of a DW along the wire is turned on and off either in phase or out of phase with the modulation field, depending on the sign of the bias field. A lock-in amplifier phase locked to the modulation source [Fig. 5(a)] was used to detect the modulated dc level of the wall-induced voltage while rejecting the (unmodulated) rf pickup. If the bias field is slowly swept from negative to positive, then any residual inductive pickup at the modulation frequency should remain constant while the signal from DW motion in the nanowire should correlate with crossings of the injection field threshold of the device.

Experiments were first performed using the two drive-field waveforms shown in Fig. 6(a). Both waveforms consisted of 20 Oe amplitude square waves with a half period $T_{1/2}=1.5$ μs, sufficiently long to drive any injected DW along the entire length of the nanowire. One of these waveforms also included injection pulses. The Kerr signal on the nanowire, averaged over many reversal cycles and normalized to the value for 60 Oe square-wave drive field, was used to evaluate the probability of DW injection by these waveforms as a function of applied dc bias field. As seen in Fig. 6(b), in the absence of the injection pulses, the Kerr signal is always zero, indicating that regardless of bias field offset, at

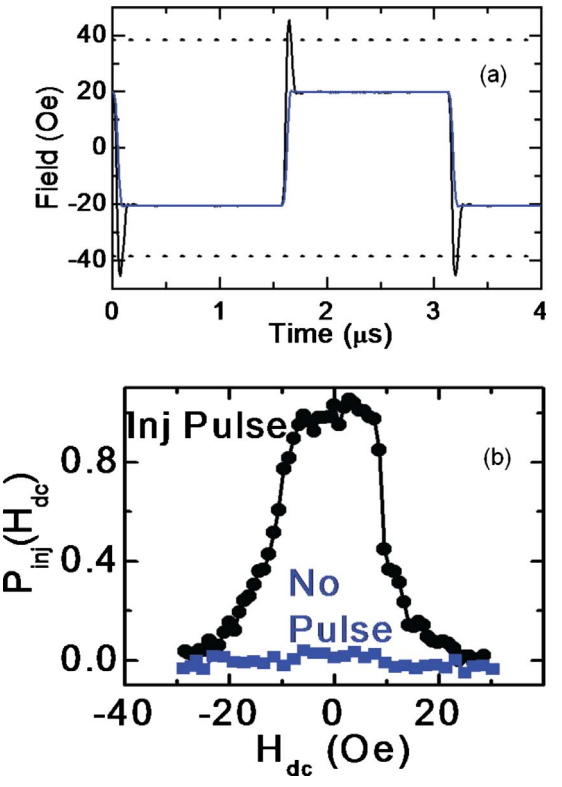

FIG. 6. (Color online) (a) High-frequency drive-field waveforms with and without a 45 Oe injection pulse. (b) Normalized Kerr signal amplitude for each waveform as a function of dc bias field.

least one side of the drive-field cycle never exceeds the injection threshold and so the nanowire magnetization never reverses. When injection pulses are added, a DW is injected with probability $P_{inj}=1$ for both halves of the drive-field cycle. However, the injection probability drops to zero for $H_{bias}>20$ Oe, indicating one side of the drive-field cycle drops below the injection threshold. Thus, the modulation field with amplitude $H_m=11$ Oe, when combined with a bias field $H_{bias}=H_m$, should periodically switch the DW injection probability between 1 and 0. This modulation is in (out of) phase for $H_{bias}<0$ ($H_{bias}>0$).

To test for evidence of domain-wall-induced voltage, a square-wave modulation field of amplitude $H_m=11$ Oe was applied together with each of the drive-field waveforms of Fig. 6(a). The measured lock-in voltage signal V_L in phase with the modulation field is shown versus the slowly swept bias field $H_{\rm dc}$ in Fig. 7(a). The large voltage offset is due to inductive pickup of the modulation field by the measurement loop and it scales linearly with the modulation field frequency and amplitude. On top of this offset is a small $H_{\rm dc}$-dependent component. As described above (see Fig. 5) any modulated voltage contribution that depends only on the magnitude of the total field will manifest as an odd function of $H_{\rm dc}$. Likewise, a voltage that depends on the sign of the field (or, in the case of inductive pickup, the sign of its time derivative) manifest as an even function of $H_{\rm dc}$. For the data in Fig. 7(a), when the drive-field waveform lacks injection pulses, V_L is symmetric about $H_{\rm dc}$. However, we find a distinct change in symmetry when injection pulses are included in the drive-field waveform. This is the signature of domain-wall induced voltage; comparing Figs. 5(c) and 5(d), the modulated DW voltage has the same amplitude for $\pm H_{\rm dc}$ but it is in phase with the modulation field for negative bias, and out of phase for positive bias. This phase difference implies a sign change in the DW contribution to V_L.

Figure 7(b) shows the odd component $\tilde{V}_L$ for each curve in Fig. 7(a). We observe a component with this symmetry only in cases in which the drive-field waveform is able to inject domain walls. The contribution by these propagating domain walls to the detected lock-in voltage V_L should be proportional to the difference in P_{inj} between the positive and negative phases of the modulation cycle, weighted by the average DW-induced voltage in each of those phases. Figure 7(c) shows $[P_{inj}(H_{\rm dc}+H_m)-P_{inj}(H_{\rm dc}-H_m)]$ versus $H_{\rm dc}$ for the drive-field waveform of Fig. 7(a) with injection pulses. Using this curve together with the mobility curve of Fig. 4(b), we have computed the expected voltage profile assuming a domain-wall-induced emf in accord with Eq. (26). Here we assume that above breakdown field H_W, a propagating DW generates a voltage of 10 nV/Oe while it propagates along the wire under the action of the total instantaneous field $H_{drive}+H_m+H_{\rm dc}$. The average voltage generated during the positive and negative cycles of the modulation field was computed, and weighted by the duty cycle of the signal (i.e., the ratio of the domain-wall transit time to the period of the drive field). The result is shown in Fig. 7(d). The measured odd component of V_L follows this curve quite closely. Based on its symmetry and its correlation with P_{inj}, we hence interpret $\tilde{V}_L$ as arising from DW motion along the nanowire.

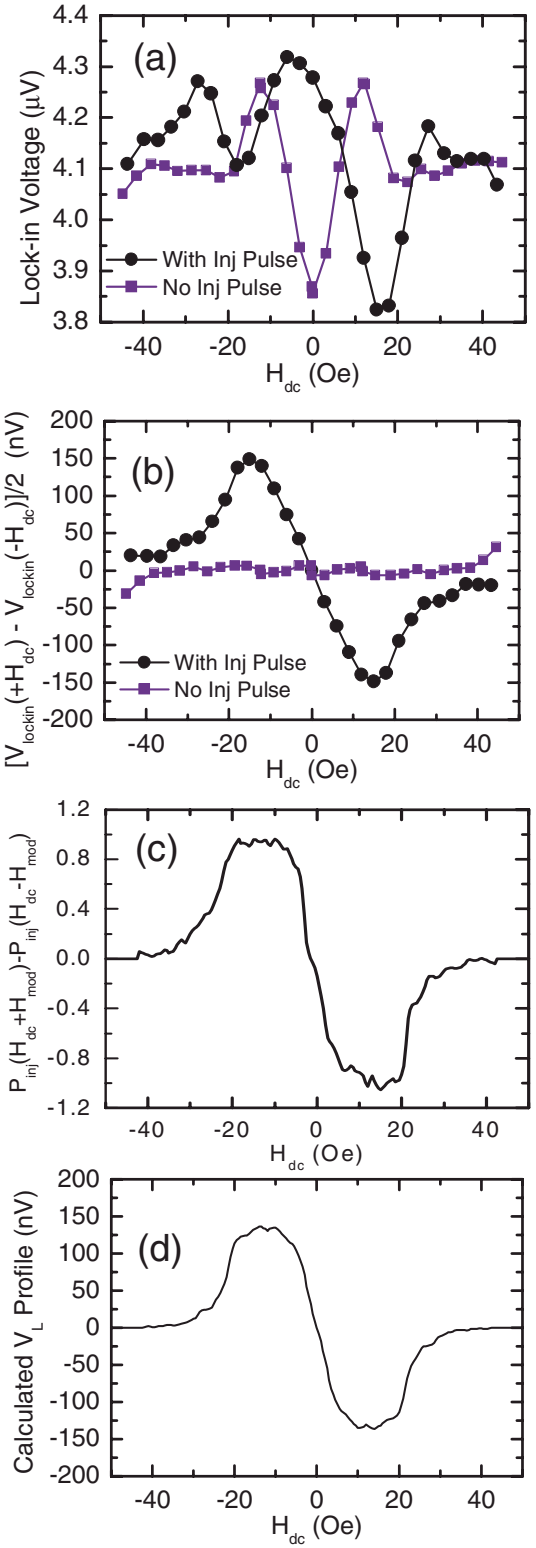

FIG. 7. (Color online) (a) Lock-in voltage V_L versus $H_{\rm dc}$ measured during application of the drive-field waveforms of Fig. 6(a) with, and without, injection pulses. (b) Odd components of the curves in (a). (c) Difference in P_{inj} between positive and negative phases of modulation field cycle, computed from an interpolation of the data in the inset. (d) Calculated dependence of domain-wall contribution to V_L based on measured injection data and DW mobility, as described in the text.

There remains an unaccounted for even component in V_L, which is present whether or not domain walls are active in the device. It is possible that domain-wall motion within the ferromagnetic contact pads also contributes to the measured signal. For purely stochastic DW motion in the pads from cycle to cycle, any such contribution would be expected to average to zero. However, pinned domain walls that are not fully expelled by the field, for example, could be driven back and forth during field cycling and contribute in a nonvanishing way. It is also possible that the inductive flux through the measurement circuit is not completely rejected by the measurement. Since the drive field and modulation field are continuously running while $H_{\rm dc}$ is swept, any inductive pickup at the modulation frequency that is proportional to dH/dt should be independent of $H_{\rm dc}$. However, due to the stray field present from the large ferromagnetic contact pads and in the vicinity of the nanowire, it is possible that the inductive flux for through the circuit contains a term proportional to dM/dt, which could add a bias field dependence to the inductive pickup term. Any such contribution depends on the sign of the total field and hence would appear as a symmetric contribution to V_L.

Several additional systematic measurements were made to verify the correlation between the odd voltage component $\tilde{V}_L$ and the behavior of the DWs presumed to lead to its appearance. The contribution to $\tilde{V}_L$ by DWs traversing the nanowire is proportional to the duty cycle given by the ratio $\tau_{\rm DW}/T_{1/2}$ [cf. Fig. 5(e)]. $\tau_{\rm DW}$ will be the same for each drive-field half cycle if we set $H_{\rm dc}=H_m$ such that the drive-field waveform has zero offset during the on phase of the modulation cycle, and each injected wall is driven by a field of amplitude $\pm H_d$ [cf. Figs. 5(c) and 5(d)]. Figure 8 shows $\tilde{V}_L$ measured at $H_{\rm dc}=H_m$ for a series of drive-field waveforms with varying period. $\tilde{V}_L$ varies inversely with $T_{1/2}$, except for $T_{1/2}<0.7$ μs, where $\tilde{V}_L$ drops precipitously. This crossover time corresponds to the independently measured wall transit time. At $T_{1/2}=\tau_{\rm DW}$, DWs generate voltage over the full duration of each drive-field cycle. For $T_{1/2}<\tau_{\rm DW}$, a DW injected into a uniform wire generates voltage during the first drive-field half period but before it reaches the end of the wire, H_d changes polarity. A new DW is injected and moves forward while the initial wall moves back, giving zero net voltage. Averaged over a full drive-field cycle, $\tilde{V}_L$ should drop, consistent with Fig. 8.

Having established the voltage component attributed to DW motion along the nanowire device, we have measured the dependence of this voltage on the drive-field amplitude. $\tilde{V}_L(H_{\rm dc})$ was also measured for a series of drive-field waveforms all with the same injection pulse as described above but with a varying plateau amplitude H_d. The measured lock-in voltage was scaled by the duty cycle (ratio of the DW transit time to the drive-field half period), along with factors to account for the spectral selection of the lock-in detector, i.e., $V_{\rm DW}=C(T_{1/2}/\tau_{\rm DW})\tilde{V}_L[H_{\rm dc}=H_m]$, where $C^{-1}=4/\pi$ is the weight of the fundamental Fourier component of a square wave. The result is plotted in Fig. 9, and shows the experimentally determined emf generated by the DW while it is being driven by a field. $V_{\rm DW}$ varies in proportion to field,

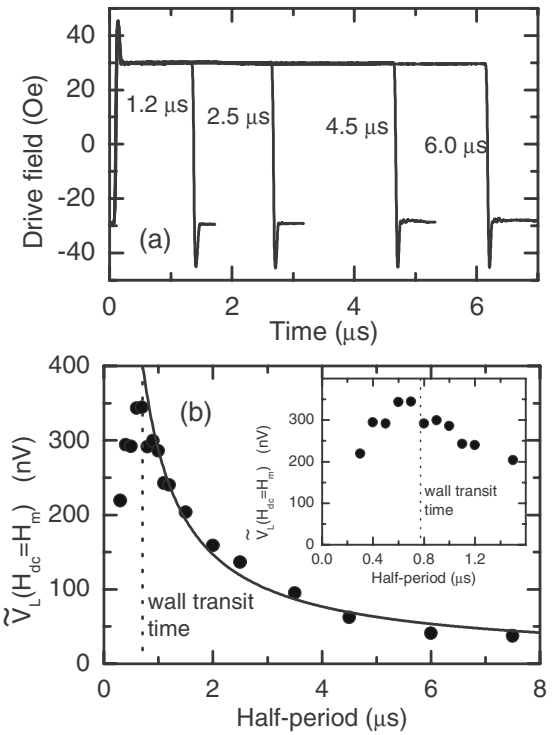

FIG. 8. Odd-symmetry component of lock-in voltage at $H_{\rm dc}=H_m$ for drive-field waveforms of varying half-period $T_{1/2}$ (half cycles shown in inset). Solid line is fit to $1/T_{1/2}$.

with a slope of $\sim$10 nV/Oe. This is close to the predicted slope $\gamma\hbar/e=11.6$ nV/Oe, and suggests a spin-polarization $P\sim 0.85$, somewhat higher than expected but within reasonable experimental bounds.

VI. DISCUSSION AND SUMMARY

In our theory, the emf is induced by the adiabatic alignment of conduction-electron spins with the local spin. Nonadiabatic processes due to spin misalignment will also contribute to the emf. Although nonadiabatic contributions will

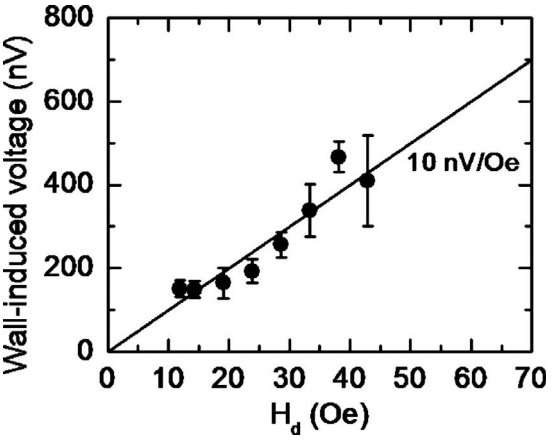

FIG. 9. Odd component of lock-in voltage at $H_{\rm dc}=H_m$ as a function of drive-field amplitude H_d, scaled as described in the text. Solid line has slope of 10 nV/Oe.

always be small compared to the topological pumping (adiabatic) contribution for wide DWs such as those in nanostrips, they could become important for narrow DWs trapped at point contacts.[29–31,59,60] We note that the pumping process is expected to cause enhanced damping of local spin dynamics,[61] closely paralleling the similar effect in magnetic multilayer structures.[40]

The topological argument with the result Eq. (12) is extremely powerful. It shows that as long as the magnetization is pinned toward opposite directions at the two ends, no matter how complicated the middle region might be, the integral of the emf over one period assumes a quantized value. This value could serve as a topological signature of the system.

For a system containing multiple DWs, if these DWs are well separated, then each DW behaves independently and the emf generated is a sum of the emf's from every single DW. When the DWs begin to interact with each other, the dynamics of the local spins become complicated, as is seen when a high magnetic field is applied.[62] In that case, the period T can be very long, hence it is more meaningful to calculate the instantaneous potential distribution by a numerical implementation of our theory combined with simulations based on the Landau-Lifshitz-Gilbert equation.

The experiment reviewed here is the first experimental detection of this emf. The measured voltage generated by a single field-driven DW is of a magnitude in accord with the predictions outlined in this paper. Because of the universal nature of this induced emf, these experiments amount to a distinct technique for quantitatively assessing the spin polarization of a ferromagnet. Improved device design is expected to further isolate spin-dynamics induced emf from extraneous sources, and new experiments are currently underway. It is, in principle, possible to measure this emf in the time domain. This type of measurement would allow for a purely electrical means for probing spin dynamics in a magnetic nanostructure. The theory and experiments outlined in this work open the door to a new avenue in which to explore spin dynamics and the coupling between local magnetic moments and conduction electrons.

To summarize, we have formulated a local gauge-invariant theory for the emf induced by DW dynamics. We have shown that it is a particular case of real-space topological pumping effects and the integral of pumped emf over one pumping period is a quantized topological invariant. Furthermore, our theory is capable of determining the whole chemical-potential distribution generated by arbitrary spin texture dynamics. The prediction of the theory has been confirmed by our experiment.

ACKNOWLEDGMENTS

The authors thank Changhai Xu, Shufeng Zhang, W. M. Saslow, and O. A. Tretiakov for valuable discussions. S.A.Y. was supported by NSF under Grant No. DMR-0906025, G.B., C.K., M.T., and J.E. were supported by NSF under Grant No. DMR-0903812, G.B. and J.E. by the Welch Foundation, D.X. and Z.Z. by the Division of Materials Sciences and Engineering (Office of Basic Energy Sciences, U.S. Department of Energy), Q.N. and A.H.M. by DOE (Grant No. DEFG03-02ER45958, Division of Materials Sciences and Engineering) and the Welch Foundation.

[1] J. F. Gregg, W. Allen, K. Ounadjela, M. Viret, M. Hehn, S. M. Thompson, and J. M. D. Coey, Phys. Rev. Lett. **77**, 1580 (1996).
[2] G. Tatara and H. Fukuyama, Phys. Rev. Lett. **78**, 3773 (1997).
[3] R. P. van Gorkom, A. Brataas, and G. E. W. Bauer, Phys. Rev. Lett. **83**, 4401 (1999).
[4] V. K. Dugaev, J. Barnas, A. Łusakowski, and Ł. A. Turski, Phys. Rev. B **65**, 224419 (2002).
[5] J. C. Slonczewski, J. Magn. Magn. Mater. **159**, L1 (1996).
[6] L. Berger, J. Appl. Phys. **55**, 1954 (1984).
[7] L. Berger, Phys. Rev. B **54**, 9353 (1996).
[8] P. P. Freitas and L. Berger, J. Appl. Phys. **57**, 1266 (1985).
[9] J. Grollier, P. Boulenc, V. Cros, A. Hamzi, A. Vaurès, A. Fert, and G. Faini, Appl. Phys. Lett. **83**, 509 (2003).
[10] M. Tsoi, R. E. Fontana, and S. S. P. Parkin, Appl. Phys. Lett. **83**, 2617 (2003).
[11] A. Yamaguchi, T. Ono, S. Nasu, K. Miyake, K. Mibu, and T. Shinjo, Phys. Rev. Lett. **92**, 077205 (2004).
[12] M. Yamanouchi, D. Chiba, F. Matsukura, and H. Ohno, Nature (London) **428**, 539 (2004).
[13] M. Kläui, C. A. F. Vaz, J. A. C. Bland, W. Wernsdorfer, G. Faini, E. Cambril, L. J. Heyderman, F. Nolting, and U. Rüdiger, Phys. Rev. Lett. **94**, 106601 (2005).
[14] M. Kläui, P.-O. Jubert, R. Allenspach, A. Bischof, J. A. C. Bland, G. Faini, U. Rüdiger, C. A. F. Vaz, L. Vila, and C. Vouille, Phys. Rev. Lett. **95**, 026601 (2005).
[15] G. S. D. Beach, C. Knutson, C. Nistor, M. Tsoi, and J. L. Erskine, Phys. Rev. Lett. **97**, 057203 (2006).
[16] M. Hayashi, L. Thomas, Ya. B. Bazaliy, C. Rettner, R. Moriya, X. Jiang, and S. S. P. Parkin, Phys. Rev. Lett. **96**, 197207 (2006).
[17] M. Yamanouchi, D. Chiba, F. Matsukura, T. Dietl, and H. Ohno, Phys. Rev. Lett. **96**, 096601 (2006).
[18] G. S. D. Beach, M. Tsoi, and J. L. Erskine, J. Magn. Magn. Mater. **320**, 1272 (2008).
[19] D. C. Ralph and M. D. Stiles, J. Magn. Magn. Mater. **320**, 1190 (2008).
[20] Y. Tserkovnyak, A. Brataas, and G. E. W. Bauer, J. Magn. Magn. Mater. **320**, 1282 (2008).
[21] P. M. Haney, R. A. Duine, A. S. Núñez, and A. H. MacDonald, J. Magn. Magn. Mater. **320**, 1300 (2008).
[22] G. Tatara, H. Kohno, and J. Shibata, Phys. Rep. **468**, 213 (2008).
[23] L. Berger, Phys. Rev. B **33**, 1572 (1986).
[24] S. A. Yang, G. S. D. Beach, C. Knutson, D. Xiao, Q. Niu, M. Tsoi, and J. L. Erskine, Phys. Rev. Lett. **102**, 067201 (2009).
[25] S. E. Barnes, J. Ieda, and S. Maekawa, Appl. Phys. Lett. **89**, 122507 (2006).
[26] S. E. Barnes and S. Maekawa, Phys. Rev. Lett. **98**, 246601

(2007).
[27] W. M. Saslow, Phys. Rev. B **76**, 184434 (2007).
[28] S. Yang, D. Xiao, and Q. Niu, arXiv:0709.1117 (unpublished).
[29] R. A. Duine, Phys. Rev. B **77**, 014409 (2008).
[30] R. A. Duine, Phys. Rev. B **79**, 014407 (2009).
[31] Y. Tserkovnyak and M. Mecklenburg, Phys. Rev. B **77**, 134407 (2008).
[32] M. Stamenova, T. N. Todorov, and S. Sanvito, Phys. Rev. B **77**, 054439 (2008).
[33] M. V. Berry, Proc. R. Soc. London, Ser. A **392**, 45 (1984).
[34] The possibility of an emf induced by a time-dependent Berry phase was first proposed in A. Stern, Phys. Rev. Lett. **68**, 1022 (1992).
[35] G. Sundaram and Q. Niu, Phys. Rev. B **59**, 14915 (1999).
[36] N. A. Sinitsyn, J. Phys.: Condens. Matter **20**, 023201 (2008).
[37] D. J. Thouless, Phys. Rev. B **27**, 6083 (1983).
[38] A. Auerbach, *Interacting Electrons and Quantum Magnetism* (Springer-Verlag, New York, 1994).
[39] N. L. Schryer and L. R. Walker, J. Appl. Phys. **45**, 5406 (1974).
[40] Y. Tserkovnyak, A. Brataas, G. E. W. Bauer, and B. I. Halperin, Rev. Mod. Phys. **77**, 1375 (2005).
[41] T. Moriyama, R. Cao, X. Fan, G. Xuan, B. K. Nikolic, Y. Tserkovnyak, J. Kolodzey, and J. Q. Xiao, Phys. Rev. Lett. **100**, 067602 (2008).
[42] R. D. McMichael and M. J. Donahue, IEEE Trans. Magn. **33**, 4167 (1997).
[43] O. Tchernyshyov and G.-W. Chern, Phys. Rev. Lett. **95**, 197204 (2005).
[44] J. Yang and J. L. Erskine (unpublished).
[45] J. Yang, C. Nistor, G. S. D. Beach, and J. L. Erskine, Phys. Rev. B **77**, 014413 (2008).
[46] Y. Nakatani, A. Thiaville, and J. Miltat, Nature Mater. **2**, 521 (2003).
[47] J. Shibata, Y. Nakatani, G. Tatara, H. Kohno, and Y. Otani, Phys. Rev. B **73**, 020403(R) (2006).
[48] M. Hayashi, L. Thomas, C. Rettner, R. Moriya, and S. S. P. Parkin, Nat. Phys. **3**, 21 (2007).
[49] O. A. Tretiakov, D. Clarke, G.-W. Chern, Y. B. Bazaliy, and O. Tchernyshyov, Phys. Rev. Lett. **100**, 127204 (2008).
[50] A. P. Malozemoff and J. C. Slonczewski, *Magnetic Domain Walls in Bubble Materials* (Academic Press, New York, 1979).
[51] A. A. Belavin and A. M. Polyakov, Zh. Eksp. Teor. Fiz. Pis'ma Red. **22**, 503 (1975) [JETP Lett. **22**, 245 (1975)].
[52] The current perpendicular to the surface of the metal must vanish. Using Ohm's law it follows that the perpendicular chemical-potential gradient also vanishes.
[53] J.-i. Ohe, S. E. Barnes, H.-W. Lee, and S. Maekawa, Appl. Phys. Lett. **95**, 123110 (2009).
[54] This Berry curvature term in ferromagnetic system was first discussed in G. E. Volovik, J. Phys. C **20**, L83 (1987).
[55] J.-Y. Lee, K.-S. Lee, S. Choi, K. Y. Guslienko, and S.-K. Kim, Phys. Rev. B **76**, 184408 (2007).
[56] S.-K. Kim, J.-Y. Lee, Y.-S. Choi, K. Y. Guslienko, and K.-S. Lee, Appl. Phys. Lett. **93**, 052503 (2008).
[57] C. Nistor, G. S. D. Beach, and J. L. Erskine, Rev. Sci. Instrum. **77**, 103901 (2006).
[58] G. S. D. Beach, C. Nistor, C. Knutson, M. Tsoi, and J. L. Erskine, Nature Mater. **4**, 741 (2005).
[59] Y. Tserkovnyak and C. H. Wong, Phys. Rev. B **79**, 014402 (2009).
[60] Kjetil Magne Dørheim Hals, A. K. Nguyen, and A. Brataas, Phys. Rev. Lett. **102**, 256601 (2009).
[61] S. Zhang and Steven S.-L. Zhang, Phys. Rev. Lett. **102**, 086601 (2009).
[62] D. J. Clarke, O. A. Tretiakov, G.-W. Chern, Ya. B. Bazaliy, and O. Tchernyshyov, Phys. Rev. B **78**, 134412 (2008).